Restricted Shock Separation in Out-of-Round TOP Nozzles

R. Stark
German Aerospace Center, Langer Grund, Lampoldshausen, 74239, Germany
S. Jack
German Aerospace Center, Lilienthalplatz 7, Braunschweig, 38108, Germany

Corresponding Author: ralf.stark@dlr.de

Abstract Thrust optimized parabola rocket nozzles can develop restricted shock separation with the associated reattachement. It becomes even more complicated when the nozzles are deformed. Detailed numerical and experimental studies were carried out to investigate the expected flow pattern. The good agreement between numerics and experiment enables reliable predictions.

1 Introduction

Flow fluctuations in or around rocket nozzles can result in structural deformations. These perturbations can be caused by combustion instabilities or ambient pressure fluctuations. In case of a separated nozzle flow, an inward-bent nozzle wall shifts the flow separation position downstream, resulting in an increased bending force. This fluid-structure interaction (FSI) is a self-reinforcing process, which might excite the nozzle eigenmodes, causing undesired damage. In the past, the German Aerospace Center (DLR) studied separated flows in ovalized truncated ideal contour nozzles (TIC) experimentally as well as numerically [1, 2, 3, 4, 5, 6]. In opposite to TIC nozzles, thrust optimized parabola nozzles (TOP), as applied in Ariane 5 and Ariane 6 rocket engines, tend to a reattached flow condition called restricted shock separation (RSS). In order to understand RSS in out-of-round TOP nozzles, a collaborative work between the Institutes of Space Propulsion and the Institute of Aerodynamics and Flow Technology, both of DLR, has been started within the framework of the in-house project TAUROS.

In conventional rocket nozzles, two types of separation pattern can be observed: the free shock separation (FSS) and the restricted shock separation (RSS). Figure 1 (left) shows the FSS characteristics. The flow in the backflow region, downstream of the actual separation, always remains detached and continous as a free jet.
During RSS, the just-separated flow reattaches again to the nozzle wall and a closed separation bubble or better ring forms, pulling the separation position downstream. Figure 1 (right) gives the RSS characteristics. The key driver for the reattachment is the momentum balance downstream of the intersection of the cap-shock pattern and the initial separation shock, where a radial momentum towards the nozzle wall can be generated. The cap-shock pattern is a consequence of the internal shock that is generated shortly downstream of the nozzle throat in TOP nozzles as well as in compressed TICs. The transition from FSS to RSS and vice versa is a highly transient process causing undesired sideloads up to 10% of the overall thrust.

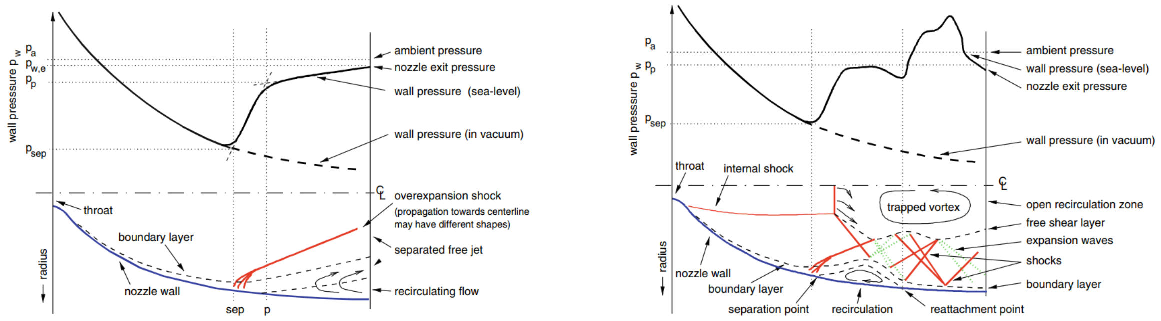

Fig. 1. Characteristics for free shock separation pattern (FSS, left) and restricted shock separation pattern (RSS, right); both taken from [7]

2 Experimental Setup

Tests were realized at cold flow subscale test facility P6.2 in Lampoldshausen, featuring dry gaseaous nitrogen as fluid, stored in 20 MPa high pressure vessels under ambient temperature. The subsequent supply system, consisting of an automatic valve, a filter, a pressure reducer, a regulation valve, and a mass flow meter, connects the fluid supply with a settling chamber that is mounted on a horizontal rig. The settling chamber is equipped with a set of grids and honeycombs to homogenize the flow. The mesh size is 4 mm^2, reducing the effective cross section down to 64%. The tested nozzle specimens were mounted downstream of the settling chamber. The facility features a maximum total pressure of $p_0 = 6$ MPa, with a maximum mass flow of 4.2 kg/s. Gaseous nitrogen is used as a working fluid to minimize condensation effects.
Prior to experiments, DLR Brunswick applied several out-of-round modes on a numerical model of the already tested DLR S1 TOP nozzle, using DLR's in-house flow solver TAU. The DLR S1 is known to assure RSS conditions during start-up as well as during shut-down of the nozzle [8]. Out of the numerically studied set, two promising candidates were chosen and manufactured in acrylic glass. The nozzles feature an oval (S1-OVAL) and a triangular shape (S1-TRI), starting downstream of a supersonic area ratio of $A_\mathrm{e}/A_\mathrm{t} = 5$, and with a maximum relative displacement of 10%, each (Fig. 2).

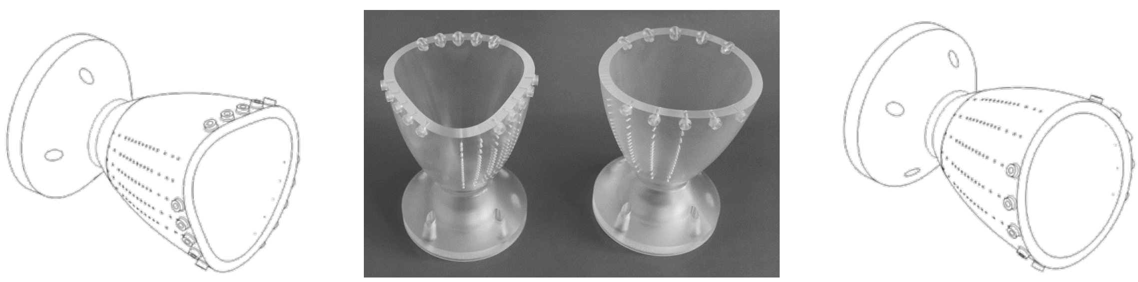

Fig. 2. Out-of-Round TOP nozzles, S1-TRI (left) and S1-OVAL (right)

Thanks to numerics, 5 axial lines with 15 optimal wall pressure port positions each could be defined in advance (Fig. 3). Via orifices (0.5 mm) drilled perpendicularly into the nozzle wall, small metal pipes and Teflon tubes, the flow was connected to piezoresistive

XT-154-190M type Kulite pressure transducers. The transducers have a measurement range of 0.1 MPa with an accuracy of 0.5% relative to the upper range limit.

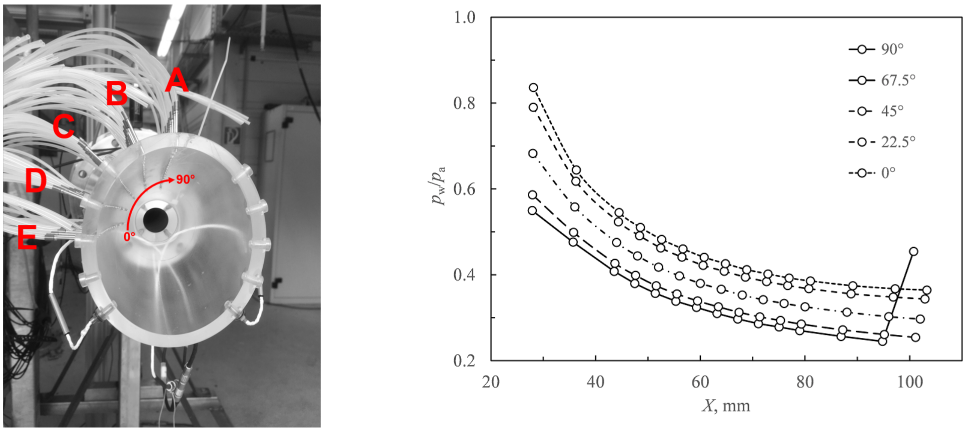

Fig. 3. View of S1-OVAL with pressure port nomenclature (left) and pressure port selection after numerical study (right)

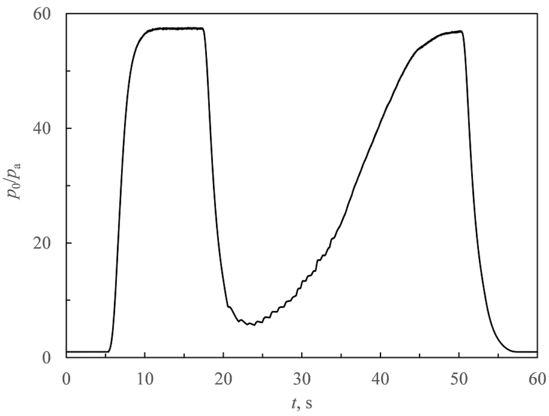

Fig. 4. Comman test sequence

The shock pattern of the nozzle exhaust jets were visualized with a classical b/w schlieren setting in z-formation [9] using a Photron Fastcam-1024PCI high-speed camera system. The schlieren images were obtained with 125 or 250 fps to record a complete test, or 3000 fps to focus on the first total pressure plateau. The nozzle specimens were rotated between the tests to capture the spatial shape of the respective exhaust jet.

For comparison reasons, all configurations were tested with the same test sequence. Figure 4 illustrates the related nozzle pressure ratio profile (NPR $= p_0/p_a$). A steep NPR increase was followed by a plateau and a steep decrease, before a medium NPR gradient phase and a second steep decrease completed the sequence.

3 Numerical Setup

The DLR TAU code was used to simulate the flow within the computational domain of the nozzles. It is a finite volume solver that solves the unsteady Reynolds-averaged Navier Stokes equations (RANS). Nitrogen as perfect gas was used as fluid model, including the respective equation of state and the viscosity model proposed by Sutherland.

To close the equation system a Reynolds stress (RSM) turbulence model was used. Within the applied RSM the production of the turbulent stress components was calculated directly from the velocity gradients. Together with the assumption of local isotropy, the dissipation term was calculated from the energy dissipation as proposed by Rotta [10]. The influence of the pressure strain onto the turbulence was related to the divergence of the velocity gradients, as proposed by Chou [11], and calculated from the turbulent quantities as proposed by Rotta [10]. A similar approach by Launder, Reece and Rodi [12] was used to calculate the pressure strain related diffusion term, supplemented by the generalized gradient hypothesis by Daly and Harlow for the turbulent velocity fluctuation influence [13]. Analogue to common two equation turbulence models, an additional scalar transport equation was used for the turbulent length scale ω (see [14]). The production of turbulent kinetic energy in the vicinity of strong shocks was limited by the empirical model developed by Karl et. al. [15]. An upwind scheme was applied for the flux vector splitting in space, using gradient reconstruction to achieve second order accuracy. The second order accurate implicit dual-time-stepping scheme by Jameson [16] was used for time integration within all transient simulations. All calculations were performed on hybrid grids of the full rotationally symmetric nozzle geometry to avoid symmetric effects forced by internal boundary conditions. The nozzle walls were assumed to be adiabatic. Earlier simulations and comparison to experimental data [1, 2, 3, 4, 6] have shown that this numerical setup is well capable to reproduce the relevant flow features in similar subscale TIC nozzles with good accuracy.

4 Results and Discussion

The test specimens were studied in different experimental configurations. The configurations differed in the combination of the connected axial rows. Care was taken that there were overlaps to ensure reliable comparability. In addition, the nozzles were rotated in order to document the nozzles' exhaust jet from several angles. The obtained experimental wall pressure results were very reproducible. Figure 5 (left) shows a comparison of the normalized experimental wall pressures and the numerical prediction.

Figure 5 (right) displays the same NPR condition but for the steep positive NPR gradient (see Fig. 4). This significantly faster process initially appears confusing. However, the reduction to the axial rows D (67.5°) and E (90°) in Fig. 6 depicts that there is a RSS condition in the bulge of the major semi-axis.

Figure 7 shows a comparison of the numerical data, represented by the density gradient magnitude plotted in planar cuts through the simulation domain (top), and experimental schlieren images (bottom) for the S1-OVAL at NPR=41. The cap-shock structure, consisting of the internal shock, the bended Mach disk and the deflected shock, as well as the separation shock and the structure of the supersonic jet are well captured by the computational setup.

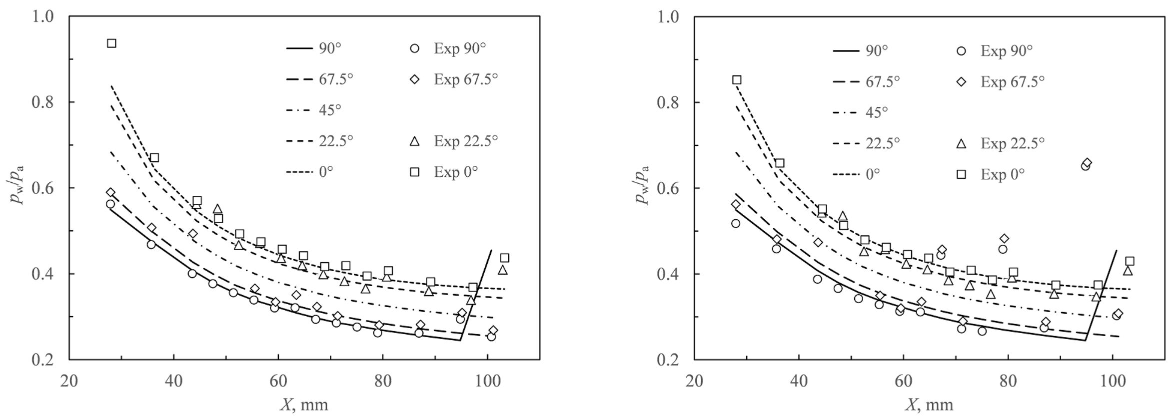

Fig. 5. Wall pressures for NPR=30, medium NPR gradient (left) and steep positive NPR gradient (right)

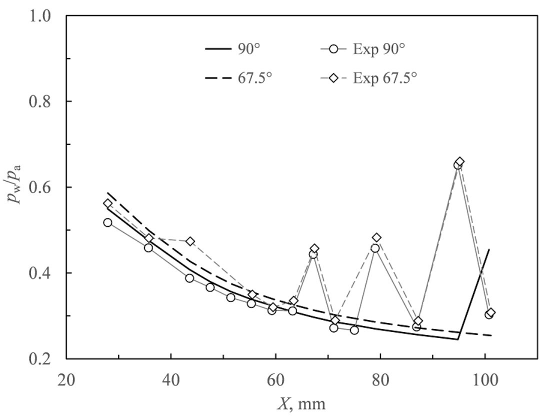

Fig. 6. Wall pressures for NPR=30, steep positive NPR gradient data selection

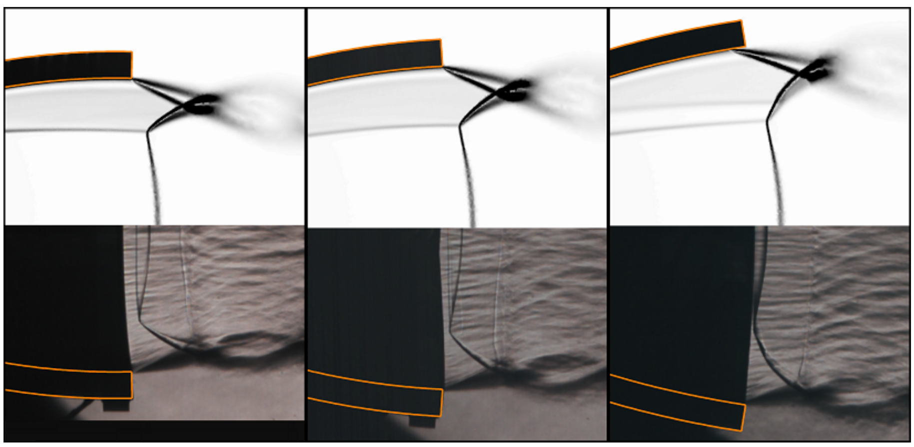

Fig. 7. Density gradient obtained from simulation results (top) and schlieren images (bottom) for S1-OVAL at NPR=41; at orientation 0°, 45° and 90° (left to right)

Compared to the schlieren images, the simulation predicts a slightly downstream shifted Mach disk position (approximately 3 mm). A comparable shift was observed in earlier investigations of TIC nozzles [2, 3, 6]. For the shown data inertia effects contribute to the difference in the shock and separation position, as the steady state simulation is compared to data obtained as a snapshot from an experimental run with transient increasing steep positive NPR gradient. Overall, the observed agreement is very satisfying and the numerical simulations are capable to correctly predict the effects of the nozzle deformation on the flow patterns.

During start-up of S1-OVAL, the flow regime undergoes two transition phases. For low NPR, free shock separation occurs, where the separation position and the shock system are located mainly inside the nozzle. While no experimental visualisation of the shocks' structure is possible for this phase, the simulations show that the oval (or generally non-rotational-symmetric) shape of the nozzle leads to a deformation of the flow pattern in the expected manner: because of the higher local expansion along the major semi-axis, the flow separates upstream of the mean position, and due to the lower expansion along the minor semi-axis, downstream of the mean position. This separation shift leads to an ovalization of the Mach disk which is stretched towards the minor semi-axis (orientation 0°) that increases with increasing NPR. At a certain NPR the supersonic jet starts to partially reattach to the wall forming a closed recirculation bubble as described in section 1. In perfectly rotational-symmetric geometries, this reattachment occurs at an arbitrary angular position and tends to move within the nozzle until finally the flow reattaches around the complete perimeter. But here, the applied geometry deformation significantly affects the described usual reattachment behavior. First, partial reattachment in the out-of-round contour occurs in the vicinity of the largest inward-bent deformation, where the distance between the supersonic jet and the nozzle wall is smallest. Because of these local effects, the partial RSS is triggered at lower NPR and its location is more stable compared to the undeformed geometry. With increasing NPR, the reattached area increases in axial and circumferential direction until the outward-directed momentum is large enough to cause an attachment along one side of the major semi-axis.

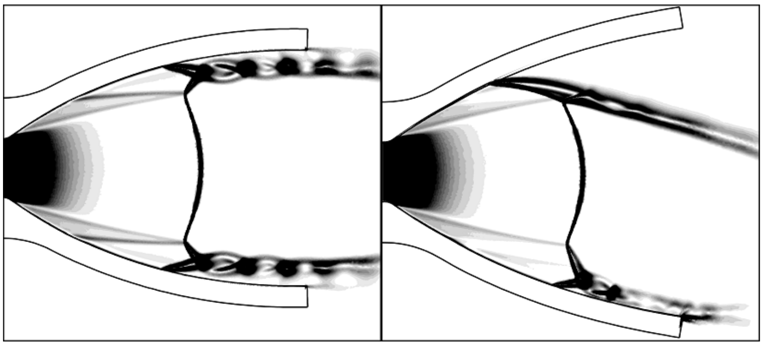

Fig. 8. One-sided RSS in transient simulation of S1-OVAL at NPR=17.39

Figure 8 shows the flow pattern of the one-sided RSS. The cut at the major semi-axis (right) points out that the supersonic jet is strongly tilted towards the reattached flow side. This tilt leads to an increased distance between the jet and the nozzle wall at the separated flow side, and completely suppresses here the developement of the cap-shock pattern. Because of the phenomena described, this one-sided RSS is stable regarding its location and leads to a strong delay to a both-sided RSS (Fig. 9), while the NPR continous to increase.

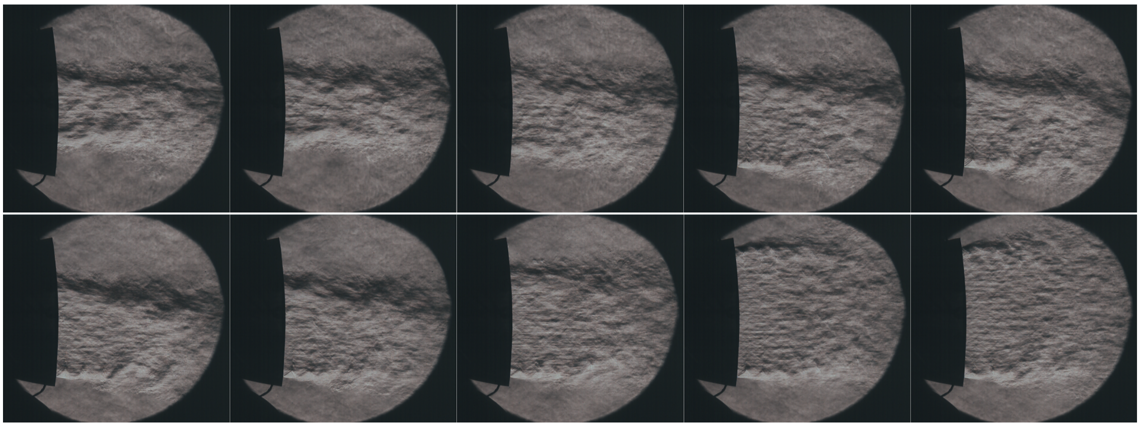

Fig. 9. Transition in S1-OVAL from FSS to one-sided RSS (top) and subsequent transition from one-sided RSS to both-sided RSS (bottom); a sequence of 5 consecusive schlieren images with 250 fps each

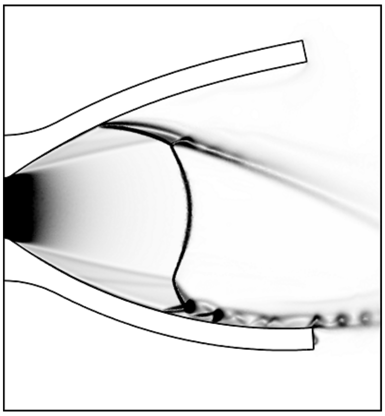

Fig. 10. One-sided RSS in transient simulation of S1-TRI nozzle at NPR=14.8

The S1-TRI behaves in a comparable way. First, the reattachement to the inward-bent nozzle wall begins, before the flow turns to the outward-bent wall; with the difference that here both adjacent outward-bent bulges are filled (Fig. 10). The third, opposite one, remains open to the ambiance. As with the S1-OVAL, this flow condition is also stable. Figure 11 documents the transition process from FSS to two-sided RSS and finally to three-sided RSS. Last but not least, Fig. 12 points out the spatial shape of the full flowing S1-TRI exhaust jet.

It should be mentioned that the existence of the aforementioned effects, especially the increased stability of the one-sided RSS, is only expected to be observed in the presented stiff nozzles. In realistic flexible nozzles the changed flow pattern, such as local reattachment or the resulting local change in the wall pressure distribution, would affect the deformation and vice versa.

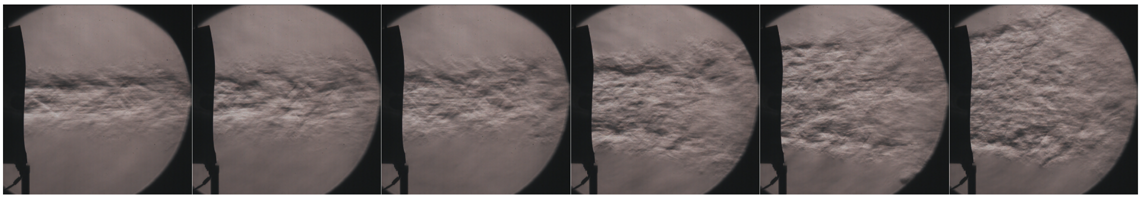

Fig. 11. S1-TRI transition process (orientation as in Fig. 10)

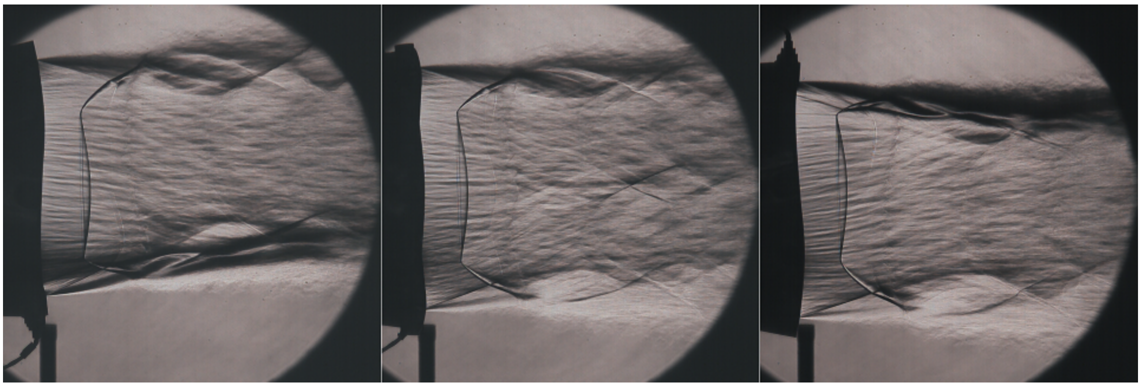

Fig. 12. Full flowing S1-TRI for NPR=56 at orientation 0°, 30° and 60° (left to right)

5 Conclusion

The numerical investigations show good agreement with the experimental results. They correctly predict the flow behavior in out-of-round rocket nozzles. Both numerical analysis and experiment show that RSS begins as expected on the minor semi-axis, but then shifts to the major semi-axis, where it remains stable. The stretched Mach disc was identified as a key driver. It has been shown that numerical simulations are capable to correctly predict the effects of the nozzle deformation onto the flow pattern.

The presented analysis helps to understand the flow response caused by initially deformed nozzle structures. These effects are expected to be observed in flexible nozzles as well, because the typical time scales at which the flow and structure react to changes in their respective counterpart differ largely due to the large difference in inertia.

6 Acknowledgments

The presented work was conducted in the framework of the German Aerospace Center (DLR) project TAUROS (TAU for Rocket Thrust Chamber Simulation) focusing on the qualification and advancement of the DLR flow solver TAU for liquid rocket thrust chamber applications. The financial support of the DLR Space Research Programmatic is highly appreciated. The authors would like to thank Nadine Smolka for her contribution, whose master thesis [17] was supervised by S. Jack.

References

[1] S. Jack and C. Génin, *Numerical and experimental investigation of flow separation in ovalized nozzles*, Space Propulsion Conference, Cologne (2014)

[2] C. Génin and S. Jack, *Flow separation study in stiff ovalized rocket nozzles, Part I: Experimental approach*, Joint Propulsion Conference, USA (2015)

[3] S. Jack and C. Génin, *Flow separation study in stiff ovalized rocket nozzles, Part II: Numerical approach*, Joint Propulsion Conference, USA (2015)

[4] C. Génin, S. Jack and R. Stark, *Flow separation in out-of-round nozzles, a numerical and experimental study*, Progress in Flight Physics **7**, pp. 269-282 (2015)

[5] C. Génin, S. Jack and R. Stark, *Flow Visualization in Out-of-Round Rocket Nozzles*, ISSW30 **1**, pp. 83-88 (2017)

[6] S. Jack and R. Stark, *Design and Preliminary Numerical Analysis of a Flexible Structure for a Cold Gas Nozzle Experiment*, FAR, Heilbronn (2022)

[7] G. Hagemann and M. Frey, *Shock pattern in the plume of rocket nozzles: needs for design consideration*, Shock Waves **17**, pp. 387–395, (2008)

[8] R. Stark and C. Génin, *Optimization of a Rocket Nozzle Side Load Reduction Device*, Journal of Propulsion and Power **32**, 6, pp. 1395-1402 (2016)

[9] R. Stark and B. Wagner, *Experimental study of boundary layer separation in truncated ideal contour nozzles*, Shock Waves **19**, 3, pp. 185-191 (2009)

[10] J. Rotta, *Statistische Theorie Nichthomogener Turbulenz*, Zeitschrift für Physik, **129**, 6, pp. 547-572 (1951)

[11] P. Y. Chou, *On Velocity Correlations and the Solutions of the Equations of Turbulent Fluctuation*, Quarterly of Applied Mathematics, **3**, 1, pp. 38-54 (1945)

[12] B. E. Launder, G. J. Reece and W. Rodi, *Progress in the Development of a Reynolds-Stress Turbulent Closure*, Journal of Fluid Mechanics, **68**, 3, pp. 537-566 (1975)

[13] B. J. Daly and F. H. Harlow, *Transport Equations in Turbulence*, Physics of Fluids, **13**, pp. 2634-2649 (1970)

[14] F. R. Menter, *Two-Equation Eddy-Viscosity Turbulence Models for Engineering Applications*, AIAA Journal, **32**, 8, pp. 1598-1605 (1994)

[15] S. Karl, J.-P. Hickey and F. Lacombe, *Reynolds Stress Models for Shock-Turbulence Interaction*, 31st International Symposium on Shock Waves, Japan, (2019)

[16] A. Jameson, *Time Dependent Calculations Using Multigrid, with Applications to Unsteady Flows Past Airfoils and Wings*, 10th Computational Fluid Dynamics Conference, USA, (1991)

[17] N. Smolka, *Numerical Study of the Influence of Deformation on Transition and Hysteresis Behaviour of Separation Mechanisms in Thrust-Optimized Parabolic Rocket Nozzles*, Master Thesis, Technical University of Berlin, (2018)